



Cite this: *Chem. Sci.*, 2023, **14**, 1155

All publication charges for this article have been paid for by the Royal Society of Chemistry

Modelling amorphous materials *via* a joint solid-state NMR and X-ray absorption spectroscopy and DFT approach: application to alumina†

Angela F. Harper, ^a Steffen P. Emge, ^b Pieter C. M. M. Magusin, ^{bc} Clare P. Grey ^b and Andrew J. Morris ^{*d}

Understanding a material's electronic structure is crucial to the development of many functional devices from semiconductors to solar cells and Li-ion batteries. A material's properties, including electronic structure, are dependent on the arrangement of its atoms. However, structure determination (the process of uncovering the atomic arrangement), is impeded, both experimentally and computationally, by disorder. The lack of a verifiable atomic model presents a huge challenge when designing functional amorphous materials. Such materials may be characterised through their local atomic environments using, for example, solid-state NMR and XAS. By using these two spectroscopy methods to inform the sampling of configurations from *ab initio* molecular dynamics we devise and validate an amorphous model, choosing amorphous alumina to illustrate the approach due to its wide range of technological uses. Our model predicts two distinct geometric environments of AlO_5 coordination polyhedra and determines the origin of the pre-edge features in the Al K-edge XAS. From our model we construct an average electronic density of states for amorphous alumina, and identify localized states at the conduction band minimum (CBM). We show that the presence of a pre-edge peak in the XAS is a result of transitions from the Al 1s to Al 3s states at the CBM. Deconvoluting this XAS by coordination geometry reveals contributions from both AlO_4 and AlO_5 geometries at the CBM give rise to the pre-edge, which provides insight into the role of AlO_5 in the electronic structure of alumina. This work represents an important advance within the field of solid-state amorphous modelling, providing a method for developing amorphous models through the comparison of experimental and computationally derived spectra, which may then be used to determine the electronic structure of amorphous materials.

Received 19th July 2022
Accepted 21st December 2022

DOI: 10.1039/d2sc04035b
rsc.li/chemical-science

Introduction

Atomic level quantum mechanical modelling has played a critical role in driving many of the advances made involving crystalline materials over the last two decades – first in terms of rationalizing materials properties, but now increasingly in predicting and optimizing both materials and devices.^{1–4} A significant challenge, however, lies in applying the same quantum mechanical methods to amorphous materials,^{4,5} despite their increasing role in devices including dielectric

layers in organic electronics, and as protective coatings across a range of materials.^{6–10}

Crystal structures, by definition, contain translational and point-group symmetries. The exploitation of these symmetries reduces the number of degrees of freedom needed to fully describe the arrangement atoms in the system, consequently making them easier to model. Amorphous structures lack the symmetries present in crystalline materials, and therefore require large simulation cells to capture the disorder of their constituent atoms, leading to very expensive or sometimes prohibitively large calculations.

To understand and ultimately improve the electronic properties of an amorphous material, it is imperative to produce an accurate, verifiable, model of its local atomic and electronic structure. In addition to the computational constraints, it is also non-trivial to validate such a model against relevant experimental structural data. Most structural determination of amorphous solids uses structure factors and radial distribution functions,^{11–14} especially on well-studied systems such as amorphous carbon, silicon, and silica. However, these provide only coarse-grained structure property relationships across the

^aTheory of Condensed Matter, Cavendish Laboratory, University of Cambridge, J. J. Thomson Avenue, Cambridge CB3 0HE, UK

^bYusuf Hamied Department of Chemistry, University of Cambridge, Lensfield Road, Cambridge CB2 1EW, UK

^cInstitute for Life Sciences & Chemistry, Hogeschool Utrecht, Heidelberglaan 7, 3584 CS Utrecht, Netherlands

^dSchool of Metallurgy and Materials, University of Birmingham, Edgbaston, Birmingham B15 2TT, UK. E-mail: a.j.morris.1@bham.ac.uk

† Electronic supplementary information (ESI) available. See DOI: <https://doi.org/10.1039/d2sc04035b>



average structure such as bond lengths, average coordination number, and bond angles. The complete structure solution of amorphous materials ultimately relies on locally sensitive, element specific techniques such as Nuclear Magnetic Resonance (NMR) and X-ray Absorption Spectroscopy (XAS). The advantage of these techniques is that they are element specific and allow for angstrom-level resolution of the atomic structure, and in the case of XAS enable the understanding of oxidation states and electronic structure.

Recent progress in machine learning has enabled models of amorphous single element structures such as silicon, carbon, and phosphorus,^{4,15–17} as well as progress in some two-element systems including HfO_2 and Li_xSi .^{3,18} In these methods, machine learning is applied to describe the atomic level interactions using training sets from density-functional theory (DFT) energy and force calculations; machine-learned models therefore have comparable radial distribution factors, bond-lengths, and structure factors to DFT-derived models with improved simulation time and length scales.³ However, their ability to predict spectral properties such as NMR and XAS with first-principles accuracy is lacking; although ShiftML predicts NMR shifts for molecular solids, its nuclei are limited to ^{13}C , ^1H , ^{15}N , ^{17}O , and ^{33}S .¹⁹ Similarly, XAS spectral lines for transition-metal oxides are predicted using a random-forest method but applied only to a set of known, crystalline, transition-metal oxides.²⁰ Clearly, there is a need for spectral predictions with first-principles accuracy, which can be applied to amorphous materials in general.

The phase-space of crystalline and amorphous alumina ($\text{am-Al}_2\text{O}_3$) is vast, with at least eight known crystalline phases, which are detailed in a series of reviews over the last two decades.^{21–23} All of the crystalline phases are characterized by the stacking of either four-fold coordinated tetrahedral Al(iv) or six-fold coordinated octahedral Al(vi) subunits. Only the amorphous phase of alumina contains five-fold coordinated Al(v) subunits, thereby distinguishing it from the crystalline phases. Experimental ^{27}Al NMR shows that the ratios of Al(vi : v : vi) environments present in amorphous alumina varies widely with synthesis technique, deposition temperature, and the substrate onto which alumina is deposited.^{24,25} Despite the large number of experimental studies showing that $\text{am-Al}_2\text{O}_3$ has several different structures, the computational literature^{26–29} is still in need of an $\text{am-Al}_2\text{O}_3$ model which is compared directly to such detailed experimental spectroscopy results; at present the only comparison is to the 1997 neutron diffraction experiments by Lamparter and Kniep³⁰ on anodic alumina.

Of the various methods for the preparation of alumina, atomic layer deposition (ALD) is one of the most common, because of the ability to deposit single atomic-layers. ALD deposited alumina has well-understood surface chemistry,^{31,32} and was first used as a high- κ dielectric material, and is now used as a coating layer across a range of electronic devices. $\text{am-Al}_2\text{O}_3$ is a wide band-gap insulator which enables surface passivation, interface stability, and protects against degradation as a coating material.^{6–8,33,34} These properties have increased the capacity retention of Li-ion battery electrodes,^{33–35} enhanced the lifetime of perovskite solar cells,^{6,36} and improved

the catalytic capabilities of metal–organic frameworks.^{37,38} Given its clear widespread applications, an atomic level model specific to ALD deposited $\text{am-Al}_2\text{O}_3$ would be indispensable to the device physics community.

This article presents our method for modelling the local structure of an amorphous material, by exploiting both first-principles calculations and high-quality experimental spectroscopy to $\text{am-Al}_2\text{O}_3$'s detailed electronic structure. The method is general and we use $\text{am-Al}_2\text{O}_3$ as an illustrative example. The novelty of our approach lies in the integration of locally sensitive experimental spectroscopy techniques with spectroscopy calculated from first principles. We obtain NMR spectra at fields up to 1 GHz, which is the current state-of-the-art in solid-state NMR, and show that our DFT-based model contains the same structural features captured by these experimental measurements. The atomic level accuracy of this model enables us to identify two distinct five-fold coordination geometries present in $\text{am-Al}_2\text{O}_3$, and the orbital character of electronic states at the Al pre-edge of the absorption spectrum, which are unique to $\text{am-Al}_2\text{O}_3$. We finally calculate an average electronic density of states (eDOS) for our model, thereby opening the door for further investigation into amorphous electronic structure.

Methods

Experimental methods

Substrates for ALD were washed with acetone, methanol/ethanol, then deionized water and blow dried with N_2 before deposition. Depositions were performed with a Picosun R-200 Advanced ALD tool attached to an MBraun glovebox. At a chamber base pressure of approximately 12 hPa the substrates were heated to 150 °C. Trimethylaluminum (TMAl, EpiValence Ltd, Electronic grade) was used as precursor gas, deionized water as reactant and N_2 as purging gas. For each cycle, corresponding to one layer, the substrates were first exposed to precursor gas (flow = 150 sccm), purged, then reactant gas (flow = 200 sccm) and finally the chamber was purged again which completes a cycle. Pulse and purge durations were 0.1 s and 10 s, respectively.

For synchrotron measurements, Al_2O_3 ALD films were deposited on pre-cut 3 mm × 3 mm Si substrates (Pi-KEM, Prime Grade, intrinsic dopant). The substrates originated from a diced 2 inch diameter Si(100) wafer ($275 \pm 25 \mu\text{m}$ thick, $>200 \Omega \text{ cm}$) single-side polished with a thermal dry oxide layer of $20 \text{ nm} \pm 10\%$ on both sides. Substrates with varying numbers of ALD layers were prepared, ranging from 2 to 1000 layers. XAS measurements shown in this work were obtained from the 1000 layer sample. Since more material was required for the NMR measurements, an 8 inch Si wafer (Picosun) was used and 1000 ALD layers were deposited. Al K-edge XAS experiments were conducted at the I09 beamline at Diamond Light Source (United Kingdom) in a total electron yield setup. Data was collected across the 1555–1600 eV range at a step size of 200 meV, using the 1.5 keV X-ray. The experimental data was then referenced against gold 4f foil using the same beamline setup.



The NMR spectroscopy measurements were performed at three different field strengths, 16.4 T, 11.8 T, and 23.5 T as detailed below. 16.4 T & 11.8 T: ^{27}Al NMR spectra were acquired using Bruker 4 mm HXY MAS probes. 1D spectra were acquired using a one-pulse pulse program with a small flip angle ($\pi/6$) on Bruker 700 MHz (16.4 T) and 500 MHz (11.8 T) magnets with Avance III consoles. Two-dimensional ^{27}Al 3QMAS (triple quantum MAS) NMR spectra were acquired on a Bruker 700 MHz (16.4 T) magnet. Quadrupolar pulse optimization was performed on $\gamma\text{-Al}_2\text{O}_3$ powder (Acros Organics). 23.5 T: ^{27}Al NMR spectra were acquired using a Bruker 1.9 mm HXY MAS probe. Spectra were acquired using a rotor-synchronised ($40\text{ kHz} \cong 2\tau = 50\ \mu\text{s}$) Hahn-echo spectrum with $p_2=2\cdot p_1 = 5\ \mu\text{s}$ ($\pi/2 = 2.5\ \mu\text{s}$) on a Bruker 1.0 GHz (23.5 T) magnet with an Avance Neo console. The MAS NMR experiments were performed at sample spinning speeds of 14 kHz (16.4 T & 11.8 T) or 40 kHz (23.5 T). The spectra were externally referenced to AlF_3 powder ($-17\ \text{ppm}^{39}$). The NMR sample was obtained by scratching off the top layer deposited on the 8 inch wafer using a Wolfram carbide pen. The powder was packed into a 4 mm (16.4 T & 11.8 T) or 1.9 mm (23.5 T) ZrO_2 rotor.

Bruker Topspin software was used for raw data handling and processing. The ^{27}Al spectra were fitted with DMFIT software⁴⁰ to obtain integrated ratios and values of average isotropic shift (δ_{iso}), average quadrupolar coupling constant (C_Q) and the chemical shift distribution (ΔCS) using the CzSimple model with $d = 5$ for the Gaussian Isotropic Model (GIM) case. The best fit is obtained using the GIM case of the Czjzek model,^{41,42} corresponding to a distribution of local environments that lead to a spread of quadrupolar coupling constants and chemical shifts.

DFT-calculated spectroscopy

Details of the methods used to generate the amorphous model are given in the Amorphous model generation section. All *ab initio* molecular dynamics (AIMD) simulations were performed using the VASP v5.4.1 DFT package⁴³ in the NVT ensemble using a Nose–Hoover thermostat⁴⁴ and with projector-augmented wave pseudopotentials with a plane-wave energy cutoff of 520 eV,⁴⁵ the PBE functional, and sampling the Brillouin zone at the Γ point. The specific pseudopotentials, parameters, and methods used to calculate the spectroscopy from first-principles are described in this section.

Both the XAS and NMR spectra were calculated on each configuration in the model independently and the outputs were summed across configurations to calculate the total spectrum. All spectral calculations, and eDOS were calculated at a plane-wave energy cut-off of 1000 eV and a single k -point at Γ in CASTEP v19.11.⁴⁶ The CASTEP gauge-inducing projector augmented wave (GIPAW) method was used to calculate all NMR parameters,^{46,47} with a PBE exchange-correlation functional and using CASTEP's on-the-fly generated ultrasoft C18 library of pseudopotentials. The NMR parameters were averaged over 45 configurations from AIMD with 48 Al atoms in each cell totalling 2160 ^{27}Al NMR chemical shift parameters for the am- Al_2O_3 model.

As ^{27}Al is a quadrupolar nuclei ($I = 5/2$), quadrupolar effects play a role in the resulting experimental NMR lineshape. However, the DFT-calculated NMR does not *a priori* include the effects of the quadrupolar nuclei in the calculation of the chemical shift parameters, and therefore we chose to additionally perform spin-simulations on each Al atom in the model, to obtain a DFT-calculated spectra including quadrupolar effects. Using the spin-simulation software, SIMPSON⁴⁸ we carried out spin-simulations on each Al atom in the model, using the same spinning speeds and magnetic fields as in the experimental NMR (4 kHz (16.4 T & 11.8 T) and 40 kHz (23.5 T)). The spin-simulations used C_Q , the isotropic chemical shift (δ_{iso}), and asymmetry parameter of the electric-field gradient (η_Q) from DFT. These spectra were obtained without including any broadening in the frequency spectrum and were subsequently broadened using a Gaussian broadening scheme to produce the spectra shown in Fig. 4.

To calculate the 2D isotropic *vs.* quadrupolar shift from the DFT-calculated NMR parameters, the quadrupolar induced shift, δ_{qs} , was calculated as follows,⁴¹

$$\delta_{\text{qs}}\left(^{27}\text{Al}\right) = -\frac{3 \times 10^4}{5} \times \frac{C_Q^2}{\nu_0^2} \left(1 + \eta_Q^2/3\right)$$

where ν_0 is the Larmor frequency in MHz. Both C_Q and η_Q are obtained from the diagonalized EFG tensor calculated using DFT. A spectrometer frequency of 182.4 MHz for ^{27}Al , corresponding to a ^1H Larmor frequency of 700 MHz, was used for ν_0 .

The total Al K-edge XAS for am- Al_2O_3 was calculated as an average across each of the 45 randomly selected configurations. In each configuration, a single Al atom was chosen as the site at which to calculate the Al K-edge XAS. The Al atoms were chosen by randomly selecting Al atoms across the configurations which satisfied the distribution of the 50%, 38%, and 12% of Al(v:v:vi) coordination environments present in the model. Each individual XAS spectrum was calculated using the core-hole pseudopotential method within CASTEP v19.11.^{49,50} To calculate the XAS for the Al K-edge, a pseudopotential with a 1s core-hole was placed on the selected Al atom and charged balanced by placing a total positive charge of +1 on the cell. The absorption spectrum was calculated at a plane-wave energy cut-off of 1000 eV, using the “hard” pseudopotential library of ultrasoft pseudopotentials in CASTEP v19.11,⁵⁰ which include an additional set of semicore states. The absorption spectrum was produced by OptaDOS and broadened using the adaptive broadening scheme.^{51–53} This spectrum was referenced using the method of Mizoguchi *et al.*⁵⁴ such that the transition energy is referenced to the difference in energy between the ground-state configuration of am- Al_2O_3 and the configuration which includes the core-hole pseudopotential.

Results

Amorphous model generation

The ideal amorphous model would comprise a highly accurate quantum mechanical description of interatomic interactions in a very large simulation cell. However, first-principles quantum mechanical calculations using DFT scale as $O(N^3)$ making these

large cell calculations unfeasible. Hence amorphous modellers choose a tradeoff between large supercells which have a high degree of disorder but with atomic interactions described by classical interatomic potentials, or smaller cells at a quantum mechanical level of theory, and a limited description of the structural disorder. Thus, all previous models of amorphous alumina from first principles are on the order of 50 to 200 atoms, and any observables such as the eDOS or chemical shift consider only a single unit cell.^{28,55-57}

Experimental ^{27}Al NMR on alumina shows that the amorphous structure is very sensitive to synthesis properties including temperature, substrate and deposition type.²⁴ However, most models of am-Al₂O₃ in the literature^{26-29,56} only validate their model against the radial distribution function (RDF) from the Lamparter *et al.* 1997 study on am-Al₂O₃ prepared by anodization.³⁰ Given the known interdependence between structure and deposition conditions, especially in the case of amorphous alumina, a direct comparison is imperative, as we will show herein.⁵⁸

In contrast to previous methods for modelling am-Al₂O₃, our method, outlined in Fig. 1, is both specific to a single experimental setup and combines configurations from across AIMD simulations. Both the DFT-calculated NMR and XAS spectra for our model match experimental results for ALD deposited alumina. Rather than choosing one configuration from AIMD, we select a range of static configurations which, when combined, contain local orderings that are representative of ALD deposited am-Al₂O₃.

To build this model, we first generate a large set of AIMD simulations using a melt-quench technique which span a range of initial conditions (densities, equilibration temperatures, and rate of equilibration) as outlined in Fig. 1 configuration

generation. For each set of initial conditions, the AIMD simulations are repeated from different starting structures, thereby exploring additional local structural orderings. For the am-Al₂O₃ model, we generated 18 initial conditions, with 3 starting structures of 120 atoms each to generate a total of 54 000 static configurations. A 120-atom model was used for each AIMD simulation to allow for computational efficiency, given the computational intensity of both NMR and XAS in DFT. We simulated am-Al₂O₃ at densities of 3.18, 3.30, and 3.42 g cm⁻³, equilibration temperatures of 300, 600, and 900 K, and using two different equilibration rates (the combination of these parameters results in 18 distinct initial conditions).

Each set of initial conditions was chosen based on literature of am-Al₂O₃ to narrow our starting search space. The density range was chosen based on previous experimental literature on am-Al₂O₃ which suggests a range of possible densities between 3.05 to 3.40 g cm⁻³.^{56,59} Although models at lower densities, such as the Lizárraga *et al.* 2.9 g cm⁻³ model, exist, such low density models often contain AlO₃ environments.^{26,60} The ^{27}Al NMR and Al K-edge XAS on am-Al₂O₃ both in this manuscript and in the literature on ^{27}Al NMR,^{61,62} shows no clear evidence for threefold coordinated Al environments, and therefore we chose to exclude any low density models which would promote AlO₃ formation. The two equilibration rates, which we refer to as a 'cooling' and 'quenching', are in line with two distinct schemes of amorphous model generation found in the literature.^{29,56} The 'cooling' method is more commonly used,^{26,56} as slower cooling rates have been shown to give better results in line with experiment, however the 'quenching' method used on a slab model of am-Al₂O₃ and Al resulted in an am-Al₂O₃ model with similar RDFs to experiment,²⁹ prompting us to also explore this scheme.

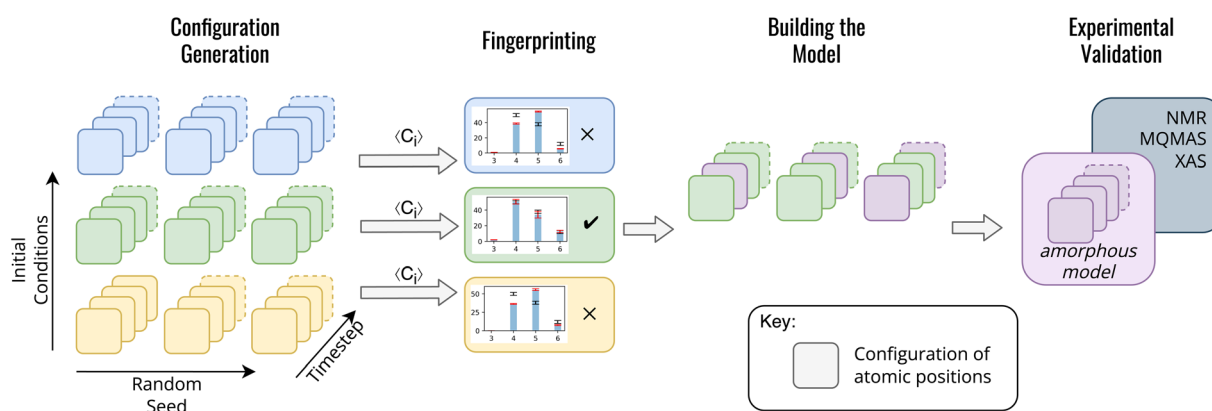


Fig. 1 Method for generating an amorphous model from a series of static configurations from AIMD. Configuration generation: each colored box represents a single static configuration from an AIMD simulation, and their depth into the page represents the number of configurations over time (timestep arrow). These configurations are colored by their initial conditions (temperature, density, and rate of equilibration) such that blue, green, and yellow are three different sets of initial conditions. The three repeated sets of configurations represent repeated AIMD simulations for each set of initial conditions. Fingerprinting: the results of simulations for each set of initial conditions are averaged across the final equilibrated 1000 AIMD steps of the simulation, and the ratios of the coordination environments are compared between the simulation and experiment. Averages over configurations which match experimental data are then used for building the model. The model consists of a total of 45 randomly selected configurations (15 from each individual AIMD simulation out of the 3 randomly seeded AIMD simulations). This model is collated and shown as the purple squares labeled 'amorphous model'. These 45 configurations are then used in the experimental validation in which the total observable is calculated as an average over the static configurations in the amorphous model.



For each initial condition, 120 atoms with stoichiometry Al_2O_3 were packed into a cubic simulation cell, using Packmol.⁶³ The cell was then melted at a temperature of 4000 K for 10 ps (5000 AIMD steps with a 2 fs time step). In the ‘cooling’ scheme, the cell was then cooled over 10 ps to the desired equilibration temperature using the Nose–Hoover thermostat, whereas when using the ‘quenching’ scheme, the cell was immediately equilibrated from the melt for a further 10 ps.

The radial distribution functions (RDF) from the final 1000 timesteps of each equilibration from AIMD was compared to the Lamparter *et al.* RDF³⁰ in the ESI Fig. S3.† Interestingly, a majority of our models each with different densities, equilibration temperatures, and cooling schemes have comparable RDFs with experiment, demanding a further narrowing of this initial set of data to obtain a model which is specific to the experimental ALD deposited am-Al₂O₃. This striking similarity between RDFs for am-Al₂O₃ despite the range of initial conditions highlights a major advantage of our method over previous methods for modelling am-Al₂O₃ (and indeed many other

amorphous structures). All previous am-Al₂O₃ models^{26,28,55,56} use RDF as the sole metric for verifying that the structure is comparable to experiment. However, the results highlighted in Fig. S3† indicate that the RDF alone is not a clear indicator of structural difference between models.

We introduce a Fingerprinting step to identify a model which is specific to ALD deposited am-Al₂O₃ (Fig. 1). Rather than compared to the experimental RDF, we use the ratio of four-five- and six-fold Al environments (Al(iv), Al(v) and Al(vi)), extracted from the experimental ²⁷Al NMR spectrum for ALD deposited am-Al₂O₃. The ratio of Al(iv : v : vi) within the ALD deposited am-Al₂O₃ are 50%, 38%, and 12% \pm 2%, respectively (Fig. 2, 3, and S1, S2†). The concentrations of these coordination environments are extracted by fitting the one-dimensional (1D), one pulse ²⁷Al NMR spectrum obtained at 16.44 T using the Czjzek model as described in the Experimental methods section and discussed in more detail below. Intensity ratios for the Al(iv : v : vi) coordinated environments of 51 : 41 : 8 and 56 : 34 : 10 were obtained at lower and higher fields respectively (Fig. 4

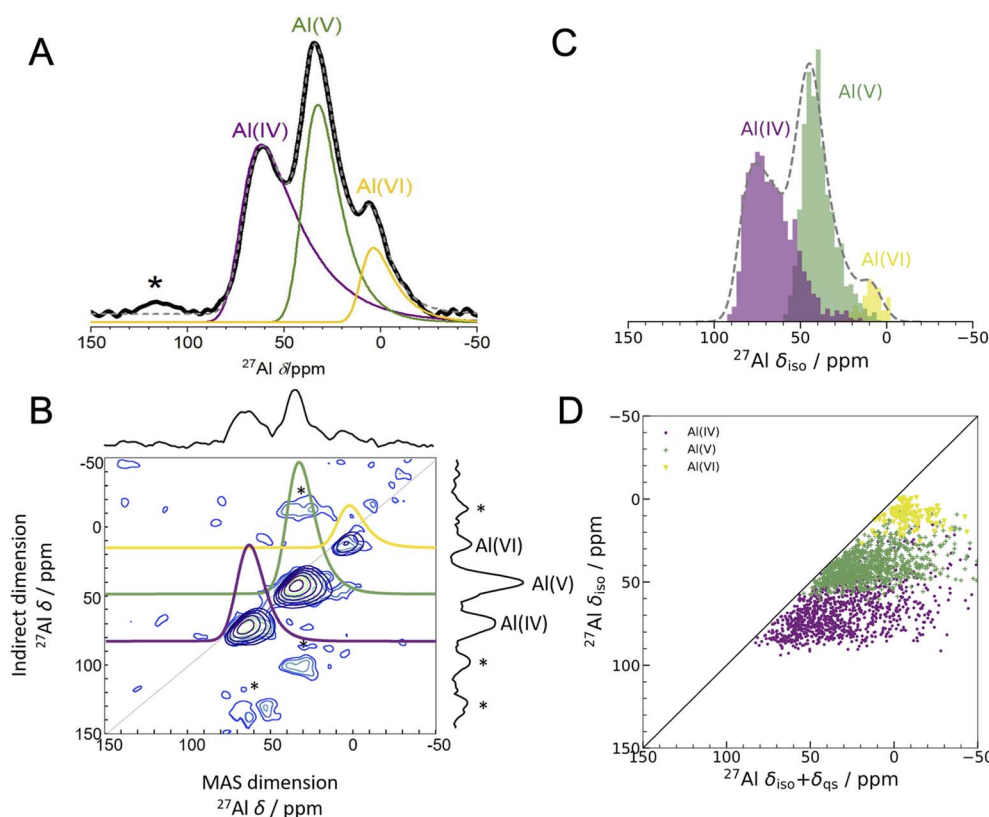


Fig. 2 Experimental 1D NMR and MQMAS compared to DFT-calculated isotropic chemical shifts (A) 1D ²⁷Al experimental NMR (black) at 16.44 T with three fits using the Czjzek model (solid lines; see Experimental methods and Table S3† for fitting parameters) a model commonly applied to spectra of quadrupolar nuclei such as ²⁷Al when the materials are disordered.^{41,42} The fits are summed to produce overall 1D spectra (dashed grey) of ALD deposited am-Al₂O₃. Spinning sidebands are indicated with an asterisk. Each signal is colored according to the closest geometric environment, based on experimental shift values for Al(iv : v : vi). (B) MQMAS at 16.44 T of ALD deposited am-Al₂O₃ shows that Al(iv) and Al(v) both have large quadrupolar shifts in the MAS dimension. (C) GIPAW NMR DFT-calculated spectrum of am-Al₂O₃. The distributions of Al environments are shown as a histogram, with the total spectrum shown in grey and Gaussian broadened to guide the eye and allow comparison with panel (A). This is a histogram showing only the chemical shifts, δ_{iso} , and neglecting the effects of the second-order quadrupolar interaction (shown in Fig. 4). (D) Comparison of δ_{iso} and $\delta_{\text{iso}} + \delta_{\text{qs}}$ from DFT-calculated NMR where δ_{qs} is calculated using the method from Engelhardt.⁴¹ This method again shows distortions in the quadrupolar dimension for both Al(iv) and Al(v), which is consistent with the MQMAS in (B). The distribution of $\delta_{\text{iso}} + \delta_{\text{qs}}$ indicates that quadrupolar effects play a large role in the experimental 1D lineshape.



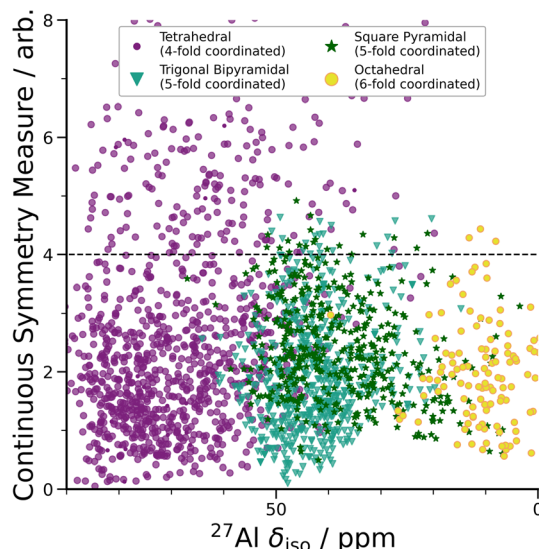


Fig. 3 DFT-calculated isotropic chemical shifts compared to the distortion of its geometric environment. GIPAW NMR calculated δ_{iso} vs. CSM as defined by ChemEnv.⁷⁰ Each coordination environment is broken down into its closest geometric environment and coordination number: Al(iv) sites were classified as tetrahedral, Al(v) sites were subdivided into trigonal bipyramidal and square pyramidal and Al(vi) as octahedral. There are a large number of distorted (CSM > 4) tetrahedral environments, which have a range of δ_{iso} shifts.

and Table S3†) suggesting that experimental errors are slightly larger than $\pm 2\%$. We have, however, chosen to take the values determined from the intermediate field spectrum because this has the highest signal to noise and, unlike the high field spectrum, was acquired with a one-pulse spectrum.

All AIMD simulations that do not have concentrations of Al(iv:v:vi) within the experimental tolerances ($\pm 2\%$) are then excluded. What remains are AIMD simulations comprising configurations which capture the specific local environments of am-Al₂O₃; we designed this approach as a way to incorporate more informative experimental data to narrow down the configuration space of simulations to those that are most likely to capture the properties of ALD deposited am-Al₂O₃.

Of the 18 initial conditions considered, just two AIMD simulations have ratios of Al(iv:v:vi) within $\pm 2\%$ error of the experimental 1D NMR data. These are the set of simulations run at 600 K and 300 K using the ‘cooling’ scheme at a density of 3.18 g cm⁻³. The results for the 300 K model are shown throughout the main text and the 600 K results are shown in the ESI† with comparable resulting DFT-calculated spectra. The other 16 models, while also within the initial range of possible experimental conditions, do not compare well to our specific ALD coating of 1000 layers of am-Al₂O₃, but could possibly be used in future work to model other phases of am-Al₂O₃ with different ratios of Al coordination.

We construct the amorphous model as a set of randomly selected static configurations compiled from the AIMD simulations which met the Fingerprinting criteria. A set of 15 configurations across the final 1000 timesteps were randomly chosen from each of the 3 AIMD simulations for the 300 K

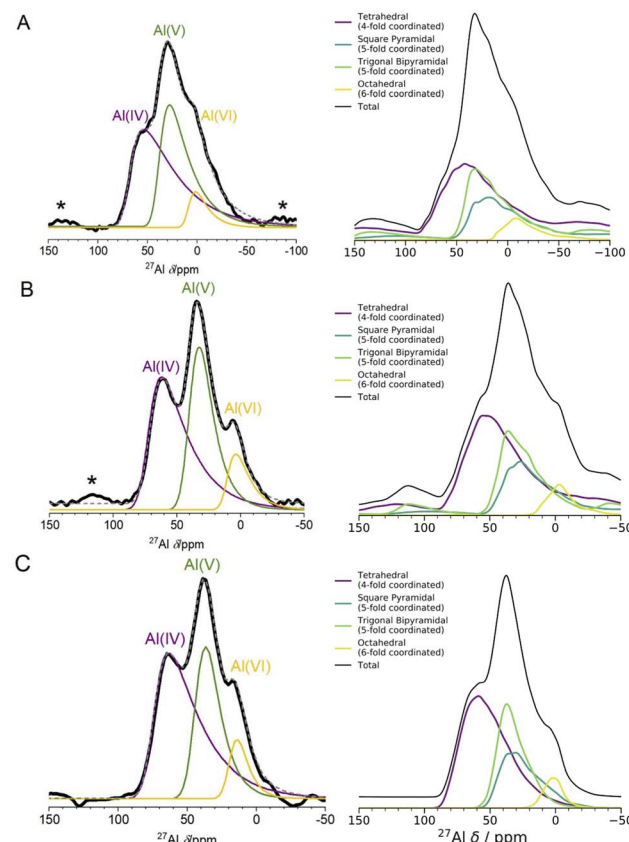


Fig. 4 1D ^{27}Al NMR experimental one pulse spectra at 3 fields and DFT computed spectra. The left panel shows experimental 1D NMR spectra measured at 3 different fields ((A) 11.75 T, (B) 16.44 T, (C) 23.49 T). The spectra in (A) and (B) were measured using a one pulse sequence, and the spectrum in (C) was measured using a Hahn-echo pulse sequence. Spinning sidebands are marked with an asterisk (*), and the fittings for each Al coordination environment were performed using the Czjzek model.^{41,42} The right panel shows the results of spin-simulations at the same 3 fields with quadrupolar lineshapes included using SIMPSON.⁴⁸ DFT-calculated δ_{iso} , η_Q and C_Q were used as input for the spin-simulations. DFT-calculated spectra show Al(v) lineshapes separated into square pyramidal and trigonal bipyramidal environments. Although the DFT/SIMPSON calculated lineshapes are broader than the experimental lineshapes, we can see a trend from low to high field that the individual environments have sharper peaks. This is expected, as higher field NMR is able to better resolve individual contributions from quadrupolar nuclei.

3.18 g cm⁻³ ‘cooling’ scheme model. The final amorphous model is the set of the 45 randomly selected configurations. Calculations of material properties are then obtained as an unweighted average over these 45 configurations. Finally, a check was added to ensure that the 45 randomly selected configurations retained the same coordination environment ratios as the original Fingerprinting step.

DFT-calculated spectroscopy on am-Al₂O₃

For some observable property, X , such as the NMR chemical shift or XAS absorption energies, we can calculate its average value across a set of static configurations (N_c) as,



$$X(N) = \sum_{c=1}^{45} X(N_c).$$

This is analogous to an ensemble average of the property in which the probability of each configuration is equally likely, as is the case for an amorphous solid with no symmetry equivalence. The ensemble average NMR and XAS spectra were calculated across the 45 configurations of am-Al₂O₃ in our model, and compared to experimental results from the 1000 layer sample of ALD deposited am-Al₂O₃. Reproducing these experimental signatures indicates that this model captures the local order, and electronic properties of the experimental amorphous phase.

The experimental ²⁷Al 1D NMR spectrum shown in Fig. 2A has 3 distinct peaks corresponding to disordered Al(iv), Al(v) and Al(vi) Al coordination environments present in a ratio of approximately 50%, 38%, and 12% \pm 2% respectively, as determined from the fits to the 1D NMR 16.44 T spectrum shown in Fig. 2A. The presence of the Al(v) signal at 41 ppm and the low intensity of the Al(vi) signal at 11 ppm are strong indicators of the amorphous nature,^{64,65} and the Al(iv) signal at 74 ppm is also characteristic of am-Al₂O₃. It is expected that a distribution of distorted Al(iv:v:vi) environments, combined with the quadrupolar nature of the ²⁷Al nucleus, would lead to large quadrupolar coupling constants and a wide range of isotropic chemical shifts. This is confirmed by the broad asymmetric peaks shown in the 1D NMR spectrum in Fig. 2A and in all three spectra in Fig. 4. Fits to the 1D spectrum using a Czjzek model capture the distribution in C_Q by fitting the spectra with a Gaussian distribution in the values of the three orthogonal components that describe the electric field gradient tensor. The average magnitudes for C_Q , $\langle |C_Q| \rangle$, were extracted using the Czjzek model as 10.9, 7.8 and 7.9 MHz for the Al(iv), (v) and (vi)-coordinated sites, respectively, at a field of 16.4 T (Table S3†). Within the Czjzek model, the standard deviation, σ , for the distribution of values of C_Q is approximately $\langle |C_Q| \rangle / 1.995$. For the Al(iv) site, σ is 5.5 MHz and C_Q ranges from zero to above 20 MHz.⁶⁶ The experimental 2D MQMAS (multi quantum MAS) NMR (Fig. 2B) contains three signals spreading along the isotropic diagonal line and horizontally along the MAS dimension, also highlighting the spread of quadrupolar coupling constants and a chemical shift distribution in the experimental am-Al₂O₃ sample.

The experimental quantification of ²⁷Al NMR is known to be a challenging task due to the presence of large quadrupolar parameters and highly distorted Al sites which lead to broadened signals from NMR.^{61,67} Further details of the experimental fitting parameters from Fig. 2 and 4 can be found in the ESI section S2.† In addition, a five-component fit was constructed, to account for “NMR invisible” Al components in the 3QMAS experiment (compared to the 1D NMR) at 16.44 T and is shown in Fig. S6.†

The DFT-calculated NMR isotropic chemical shifts for each configuration in the amorphous model reproduce the total isotropic range and location of shifts in the experimental 1D spectrum (Fig. 2C). The 1D NMR has three main peaks,

identified by the Al(iv:v:vi) environments, with δ_{iso} at 74, 45, and 10 ppm in DFT and 74, 41, and 11 ppm in the experiment shown in Fig. 2A. In addition, the calculated quadrupolar induced shifts shown in Fig. 2D have wide distributions especially in the Al(iv) and Al(v) sites. The calculated δ_{qs} shift is primarily influenced by the magnitude of C_Q , indicating a large distribution of quadrupolar coupling constants. The DFT-calculated C_Q values for Al(iv) sites ranges from zero to 25 MHz, and for Al(v) sites is zero to 20 MHz (shown in Fig. S7†), while for Al(vi) sites the range is smaller from zero to 15 MHz. A similar distribution of high C_Q values for Al(iv) and Al(v) sites is found in both aluminosilicate glasses and sol-gel prepared MgO-Al₂O₃ and ZrO₂-Al₂O₃.^{68,69}

A wide range of C_Q values is an indicator of distorted Al environments within the sample. One advantage of calculating the NMR spectrum using DFT, is that the chemical shift tensor is calculated for each atom in the model. We can therefore construct spectra based on atom-specific coordination environments. Using a continuous-symmetry measure (CSM),⁷⁰ a measure of the relative distortion of each Al environment from its closest geometric environment was extracted for each site in the model. A comparison of the CSM to isotropic chemical shift (Fig. 3), shows that most Al(iv) sites are distorted from a tetrahedral geometry (CSM > 4).⁷⁰ Distorted sites give rise to larger C_Q values, and therefore this wide range of distorted Al(iv) sites is in agreement with the wide range (zero to 25 MHz) of the DFT-calculated C_Q values for Al(iv).

Separating the DFT-calculated 1D NMR spectrum into the closest geometric environment, as shown in Fig. 3, determines that two types of Al(v) environments, square pyramidal and trigonal bipyramidal, exist within the am-Al₂O₃ model. The signal from these two sites combine to form the Al(v) peak in the 1D NMR at 41 ppm, with a range of site-specific shifts from 20 to 60 ppm. Both these Al(v) sites are less distorted, on average, than the Al(iv) sites reflecting their slightly smaller distributions in C_Q values. There is limited experimental literature on the two geometric Al(v) environments, as their spectra are not easily deconvoluted from (experimental) 1D ²⁷Al NMR.⁶² The model of am-Al₂O₃ from DFT enables the construction of these two sites' spectra, while their overlapping ²⁷Al δ_{iso} values results in one single Al(v) assignment in the experimental 1D spectrum.

The spin-simulation tool SIMPSON⁴⁸ was used to incorporate quadrupolar interactions into the DFT-calculated shifts at three fields (11.75 T, 16.44 T, 23.49 T) corresponding to the three fields at which the experimental NMR spectra (Fig. 4 left panel) were obtained. The resulting DFT-calculated spectra are shown in Fig. 4 (right panel) and the distribution of chemical shifts for the Al(iv) and Al(v) environments is well described. Summing together the individual spectra for each Al environment in the model results in environments with high C_Q values and low intensities leading to a long sloping tail in the resulting Al(iv) and Al(v) environments' total spectrum. This sloping tail is a feature explicitly incorporated into the Czjzek model which was used to carry out the experimental fittings for each environment. However, the DFT-calculated chemical shifts, asymmetry parameters, and quadrupolar coupling constants which are used to produce the spectra shown in Fig. 4 (right panel)



also have this same shape, indicating that the Al environments in the model are similar to those expected for amorphous systems with quadrupolar nuclei. In addition, by incorporating the magnetic-field strength into the simulation, and comparing with the experimental results at three fields, we find that higher fields show sharper peaks of the Al(iv : v : vi) environments, and a narrower overall spectral width. This is more pronounced in the experimental results, which may be partly a result of the DFT-calculated C_Q values being overestimated, leading to a broadening in the NMR peaks. This overestimation is documented in the literature on DFT-calculated EFG tensors^{61,71}

NMR probes local atomic structure, while XAS probes the local electronic structure, of am-Al₂O₃. The experimental Al K-edge XAS spectrum shown in Fig. 5, exhibits three main features; a pre-edge feature (a) and two dominant broad peaks at 1565 eV (b) and 1570 eV (c) which are similar to those in Al-rich glasses⁷² and attributed to transitions in Al(iv) and Al(vi) respectively. The absorption edge for Al(v) lies between Al(iv) and Al(vi), and has no experimental reference. Calculating core-hole spectra for all Al sites in the amorphous model, determines the location of this Al(v) absorption edge between 1565 and

1570 eV (Fig. 5), and confirms the absorption energy of the Al(iv) and Al(vi) peaks, indicating that the model's electronic structure is consistent with that of experimental am-Al₂O₃.

In addition to identifying the two main XAS peaks, the pre-peak at 1562.5 eV was also reproduced using DFT-calculated XAS. Previous experimental work on Al K-edge spectroscopy in zeolites also identifies a pre-edge at 1563 eV,⁷³ which they attribute to transitions in Al(II) sites. A pre-edge at 1565 eV is also documented for the crystalline α -Al₂O₃ phase, and assigned to 1s to 3s transitions in Al(vi) sites.^{74,75} The pre-edge in am-Al₂O₃ is at 1562.5 eV, both in experiment and in the DFT-calculated spectrum, as shown in Fig. 5, and occurs in either tetrahedral Al(iv) sites or square pyramidal Al(v) sites. DFT-calculated spectra for individual Al(iv) sites in our am-Al₂O₃ model show that the pre-edge at 1562.5 eV is a result of transitions from Al 1s to 3s states, within distorted Al environments. This transition is expected in distorted Al(iv) or Al(v) sites where the local centrosymmetry is broken, and transitions below the main absorption energy may occur. Because the configurations generated in the model of am-Al₂O₃ presented in this work were obtained from AIMD at 300 K, atomic vibrations at that temperature are naturally included in the model without the need to calculate additional dynamical effects.⁷⁴ As the Al(v) main peak at b (1565 eV in Fig. 5) is at a similar absorption energy as the Al(iv) peak, the Al(v) contributions are not separated in experiment, but are easily distinguished using XAS calculated from DFT. While such deconvolution is routinely applied in crystalline systems,^{76–79} this result demonstrates the capability of performing a similar analysis on an amorphous material.

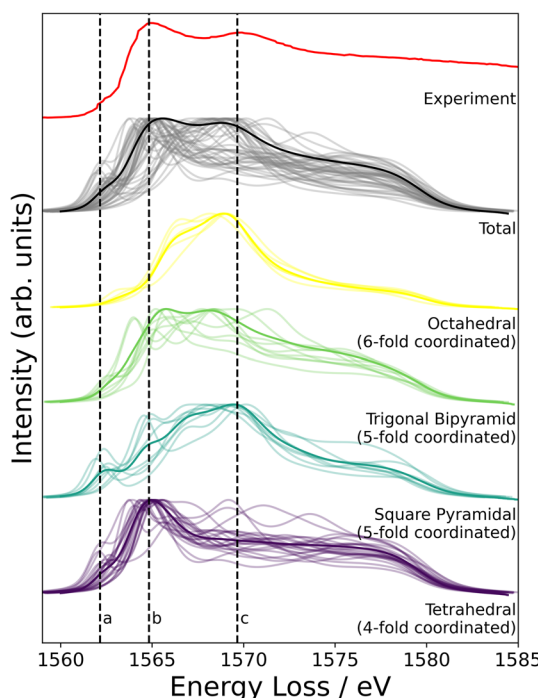


Fig. 5 Experimental XAS spectrum obtained from the ALD deposited sample compared to the calculated core-hole XAS. The experimental spectrum is shown in red, and is obtained from the 1000 layer ALD deposited sample (details in Experimental methods section). Three distinct features at 1562, 1565, and 1570 eV are denoted by dashed lines a, b, and c. The grey lines in the total spectrum from DFT show each individual spectra calculated at a single Al site from the am-Al₂O₃ model, and the solid black line is the sum of those spectra. DFT-calculated spectra separated by coordination environment are shown, colored by coordination environment; thin lines are individual spectra, thick lines are the sum for each environment. All Al(iv) sites were classified as tetrahedral, Al(v) sites were subdivided into trigonal bipyramidal and square pyramidal, and Al(vi) as octahedral.

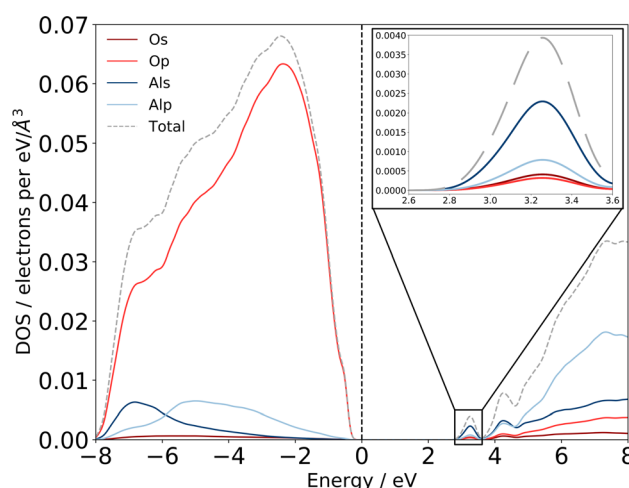


Fig. 6 Computed eDOS for amorphous alumina. Total eDOS separated by atom and orbital contribution shows that am-Al₂O₃ is a wide bandgap insulator, within PBE with a gap of 2.6 eV. States at the top of the valence band, near the Fermi level are primarily O p states, with states in the conduction-band minimum being primarily Al s (detail shown inset top right). The dashed grey line is the sum of these states, and the total eDOS was broadened using a Gaussian function of width 0.1 eV, as implemented in OptaDOS.^{51,52} The Fermi level is set to 0 eV for all configurations. Two localized states at 3.2 and 4.2 eV above the Fermi level have Al s character and mixed Al s, p character, respectively.



Previous experimental XAS on the Al L_{2,3}-edge⁸⁰ proposes that the location of the conduction band minimum (CBM) is governed by the charge transfer from Al to O atoms, specifically between the O 2p states at the valence band maximum (VBM) and Al 3s states at the CBM. We can confirm the experimental assignments of the orbital character with the electronic structure of our am-Al₂O₃ model by calculating the eDOS as an unweighted average across the 45 configurations, as shown in Fig. 6. States at the VBM are O p type character, and states at the CBM are Al s character. Interestingly, we identify two small peaks at the bottom of the conduction band at 3.2 and 4.2 eV which are low density states in this material. The computed eDOS also confirms the experimentally predicted wide band-gap insulating nature of am-Al₂O₃.^{76–79}

Conclusions

Previous work^{3,81} implies that amorphous models require thousands of atoms in the unit cell or semi-infinite simulation times to fully capture local properties. We show that by averaging across AIMD simulations and incorporating experimental insight into the sampling approach, we produce a model of am-Al₂O₃ which exhibits the same local structural properties as captured by experimental NMR and the same electronic properties as captured by XAS.

Identifying a subset of configurations from AIMD to generate the model of am-Al₂O₃, enables the calculation of electronic properties, such as the eDOS, NMR and XAS, which is not possible using classical simulation methods. This is especially important for functional materials such as alumina, which are routinely used in electronic devices. We further demonstrate the importance of incorporating experimental insight at the model configuration sampling stage, as we describe a set of 54 different AIMD simulations, all with sensible initial conditions and RDFs, but only two of which with coordination environments within the experimental margin of error. This additionally underscores the need for having a specific experimental comparison metric when generating amorphous models; the results presented in this work are all with reference to one ALD deposited sample of alumina using the most relevant possible spectroscopy methods for characterization.

This article illustrates the importance of the connection between choosing the relevant metrics (here coordination environment) for developing a model and calculating experimental observables. The method of averaging across static configurations from experimentally informed sampling of configurations from AIMD simulations can be applied to other amorphous systems, where local structure–property relationships are critical to the accurate modelling of the system. For example, in amorphous VS₄, experimental ⁵¹V NMR and S K-edge XANES show structural transformations during Li-ion battery cycling,⁸² which could be modeled using the presented method. More broadly, the class of amorphous metal oxides (among them MnO₂, Fe₂O₃, TiO₂, and a host of others) are used in energy storage applications, and their local structure and ordering of the metal oxide coordination environments plays a large role in the function and optimization of energy storage

devices.^{83,84} We hope that this work has shed light on the importance of choosing the appropriate parameters for modelling amorphous materials, and offered a new perspective on utilizing experimental spectroscopy in the modelling of amorphous phases from first principles.

Data availability

The computational data including structures, NMR, and XAS spectra, as well as the electronic DOS found in this article are published online in the Cambridge Data Repository at <https://doi.org/10.17863/CAM.92274>.

Author contributions

AF Harper: formal analysis, writing – original draft preparation, data curation, conceptualization. SE Emge: investigation, writing – review and editing. PCMM Magusin: support with MQMAS setup and analysis, organization of 1 GHz measurements. CP Grey: supervision, resources, writing – review and editing. AJ Morris: supervision, resources, writing – review and editing.

Conflicts of interest

There are no conflicts to declare.

Acknowledgements

The authors thank Steve Haws (Henry Royce Institute, Cambridge) for assistance with the ALD and Richard Chen (University of Cambridge, Chemistry) for NMR sample preparation. The authors also thank Dr Trent Franks and the UK High-Field Solid-State NMR Facility Warwick for measurements on the 1 GHz magnet. Funding: AFH acknowledges the financial support of the Gates Cambridge Trust and the Winton Programme for the Physics of Sustainability, University of Cambridge, UK. AJM acknowledges funding from EPSRC (EP/P003532/1). The authors acknowledge networking support *via* the EPSRC Collaborative Computational Projects, CCP9 (EP/M022595/1) and CCP-NC (EP/T026642/1). This work was performed using resources provided by the Cambridge Service for Data Driven Discovery (CSD3) operated by the University of Cambridge Research Computing Service (<https://dirac.ac.uk>), provided by Dell EMC and Intel using Tier-2 funding from the EPSRC (capital grant EP/P020259/1), and DiRAC funding from the Science and Technology Facilities Council (<https://dirac.ac.uk>). SPE acknowledges funding *via* an EPSRC iCASE (Award 1834544) and *via* the Royal Society (RP/R1/180147). For ALD sample preparation, use of the Ambient Processing Cluster Tool, part of Sir Henry Royce Institute–Cambridge Equipment, EPSRC grant EP/P024947/1 is gratefully acknowledged.



Notes and references

1 J. Hoja, H.-Y. Ko, M. A. Neumann, R. Car, R. A. DiStasio Jr and A. Tkatchenko, Reliable and Practical Computational Description of Molecular Crystal Polymorphs, *Sci. Adv.*, 2019, **5**(1), eaau3338, DOI: [10.1126/SCIAADV.AAU3338](https://doi.org/10.1126/SCIAADV.AAU3338).

2 S. Woodley and R. Catlow, Crystal Structure Prediction from First Principles, *Nat. Mater.*, 2008, **7**(12), 937–946, DOI: [10.1038/NMAT2321](https://doi.org/10.1038/NMAT2321).

3 G. Sivaraman, A. N. Krishnamoorthy, M. Baur, C. Holm, M. Stan, G. Csányi, C. Benmore and A. Vázquez-Mayagoitia, Machine-Learned Interatomic Potentials by Active Learning: Amorphous and Liquid Hafnium Dioxide, *npj Comput. Mater.*, 2020, **6**(1), 1–8, DOI: [10.1038/s41524-020-00367-7](https://doi.org/10.1038/s41524-020-00367-7).

4 V. L. Deringer, N. Bernstein, G. Csányi, C. ben Mahmoud, M. Ceriotti, M. Wilson, D. A. Drabold and S. R. Elliott, Origins of Structural and Electronic Transitions in Disordered Silicon, *Nature*, 2021, **589**(7840), 59–64, DOI: [10.1038/s41586-020-03072-z](https://doi.org/10.1038/s41586-020-03072-z).

5 M. Aykol, S. S. Dwaraknath, W. Sun and K. A. Persson, Thermodynamic Limit for Synthesis of Metastable Inorganic Materials, *Sci. Adv.*, 2018, **4**(4), eaao0148, DOI: [10.1126/SCIAADV.AAQ0148](https://doi.org/10.1126/SCIAADV.AAQ0148).

6 C. Das, M. Kot, T. Hellmann, C. Wittich, E. Mankel, I. Zimmermann, D. Schmeisser, M. Khaja Nazeeruddin and W. Jaegermann, Atomic Layer-Deposited Aluminum Oxide Hinders Iodide Migration and Stabilizes Perovskite Solar Cells, *Cell Rep. Phys. Sci.*, 2020, **1**(7), 100112, DOI: [10.1016/J.XCRP.2020.100112](https://doi.org/10.1016/J.XCRP.2020.100112).

7 Z. Yang, T. Albrow-Owen, H. Cui, J. Alexander-Webber, F. Gu, X. Wang, T. C. Wu, M. Zhuge, C. Williams, P. Wang, A. v. Zayats, W. Cai, L. Dai, S. Hofmann, M. Overend, L. Tong, Q. Yang, Z. Sun and T. Hasan, Single-Nanowire Spectrometers, *Science*, 2019, **365**(6457), 1017–1020, DOI: [10.1126/SCIENCE.AAX8814](https://doi.org/10.1126/SCIENCE.AAX8814).

8 J. Lu, B. Fu, M. Kung, G. Xiao, J. Elam, H. Kung and P. Stair, Coking- and Sintering-Resistant Palladium Catalysts Achieved through Atomic Layer Deposition, *Science*, 2012, **335**(6073), 1205–1208, DOI: [10.1126/SCIENCE.1212906](https://doi.org/10.1126/SCIENCE.1212906).

9 M. Fukuhara, T. Kuroda, F. Hasegawa, T. Hashida, M. Takeda, K. Konno and N. Fujima, AlO_6 Clusters' Electric Storage Effect in Amorphous Alumina Supercapacitors, *Sci. Rep.*, 2021, **11**(1), 1–6, DOI: [10.1038/s41598-021-81483-2](https://doi.org/10.1038/s41598-021-81483-2).

10 M. G. Kim, M. G. Kanatzidis, A. Facchetti and T. J. Marks, Low-Temperature Fabrication of High-Performance Metal Oxide Thin-Film Electronics via Combustion Processing, *Nat. Mater.*, 2011, **10**(5), 382–388, DOI: [10.1038/nmat3011](https://doi.org/10.1038/nmat3011).

11 Y. Yang, J. Zhou, F. Zhu, Y. Yuan, D. J. Chang, D. S. Kim, M. Pham, A. Rana, X. Tian, Y. Yao, S. J. Osher, A. K. Schmid, L. Hu, P. Ercius, J. Miao and Y. Yuan, Determining the Three-Dimensional Atomic Structure of an Amorphous Solid, *Nature*, 2021, **592**, 60–64, DOI: [10.1038/s41586-021-03354-0](https://doi.org/10.1038/s41586-021-03354-0).

12 B. Bhattachari, A. Pandey and D. A. Drabold, Evolution of Amorphous Carbon across Densities: An Inferential Study, *Carbon*, 2018, **131**, 168–174, DOI: [10.1016/J.CARBON.2018.01.103](https://doi.org/10.1016/J.CARBON.2018.01.103).

13 G. Cernuto, S. Galli, F. Trudu, G. M. Colonna, N. Masciocchi, A. Cervellino and A. Guagliardi, Investigating the Amorphous–Crystalline Interplay in $\text{SiO}_2/\text{TiO}_2$ Nanocomposites by Total Scattering Methods, *Angew. Chem., Int. Ed.*, 2011, **50**(46), 10828–10833, DOI: [10.1002/ANIE.201104149](https://doi.org/10.1002/ANIE.201104149).

14 A. Pedersen, L. Pizzagalli and H. Jónsson, Optimal Atomic Structure of Amorphous Silicon Obtained from Density Functional Theory Calculations, *New J. Phys.*, 2017, **19**(6), 063018, DOI: [10.1088/1367-2630/aa732e](https://doi.org/10.1088/1367-2630/aa732e).

15 M. A. Caro, A. Aarva, V. L. Deringer, G. Csányi and T. Laurila, Reactivity of Amorphous Carbon Surfaces: Rationalizing the Role of Structural Motifs in Functionalization Using Machine Learning, *Chem. Mater.*, 2018, **30**(21), 7446–7455, DOI: [10.1021/acs.chemmater.8b03353](https://doi.org/10.1021/acs.chemmater.8b03353).

16 V. L. Deringer and G. Csányi, Machine Learning Based Interatomic Potential for Amorphous Carbon, *Phys. Rev. B*, 2017, **95**(9), 094203, DOI: [10.1103/PhysRevB.95.094203](https://doi.org/10.1103/PhysRevB.95.094203).

17 Y. Zhou, W. Kirkpatrick, V. L. Deringer, Y. Zhou, W. Kirkpatrick and V. L. Deringer, Cluster Fragments in Amorphous Phosphorus and Their Evolution under Pressure, *Adv. Mater.*, 2021, **21**07515, DOI: [10.1002/ADMA.202107515](https://doi.org/10.1002/ADMA.202107515).

18 N. Artrith, A. Urban and G. Ceder, Constructing First-Principles Phase Diagrams of Amorphous Li_xSi Using ML Assisted Sampling, *J. Chem. Phys.*, 2018, **148**, 241711, DOI: [10.1063/1.5017661](https://doi.org/10.1063/1.5017661).

19 F. M. Paruzzo, A. Hofstetter, F. Musil, S. De, M. Ceriotti and L. Emsley, Chemical Shifts in Molecular Solids by Machine Learning, *Nat. Commun.*, 2018, **9**(1), 1–10, DOI: [10.1038/s41467-018-06972-x](https://doi.org/10.1038/s41467-018-06972-x).

20 S. B. Torrisi, M. R. Carbone, B. A. Rohr, J. H. Montoya, Y. Ha, J. Yano, S. K. Suram and L. Hung, Random Forest Machine Learning Models for Interpretable X-Ray Absorption near-Edge Structure Spectrum-Property Relationships, *npj Comput. Mater.*, 2020, **6**(1), 1–11, DOI: [10.1038/s41524-020-00376-6](https://doi.org/10.1038/s41524-020-00376-6).

21 I. Levin and D. Brandon, Metastable Alumina Polymorphs: Crystal Structures and Transition Sequences, *J. Am. Ceram. Soc.*, 2005, **81**(8), 1995–2012, DOI: [10.1111/j.1151-2916.1998.tb02581.x](https://doi.org/10.1111/j.1151-2916.1998.tb02581.x).

22 C. Vinod Chandran, C. E. A. Kirschhock, S. Radhakrishnan, F. Taulelle, J. A. Martens and E. Breynaert, Alumina: Discriminative Analysis Using 3D Correlation of Solid-State NMR Parameters, *Chem. Soc. Rev.*, 2019, **48**(1), 134–156, DOI: [10.1039/C8CS00321A](https://doi.org/10.1039/C8CS00321A).

23 M. F. Peintinger, M. J. Kratz and T. Bredow, Quantum-Chemical Study of Stable, Meta-Stable and High-Pressure Alumina Polymorphs and Aluminum Hydroxides, *J. Mater. Chem. A*, 2014, **2**(32), 13143–13158, DOI: [10.1039/C4TA02663B](https://doi.org/10.1039/C4TA02663B).

24 V. Sarou-Kanian, A. N. Gleizes, P. Florian, D. Samélor, D. Massiot and C. Vahlas, Temperature-Dependent 4-, 5- and 6-Fold Coordination of Aluminum in MOCVD-Grown Amorphous Alumina Films: A Very High Field ^{27}Al -NMR



Study, *J. Phys. Chem. C*, 2013, **117**(42), 21965–21971, DOI: [10.1021/jp4077504](https://doi.org/10.1021/jp4077504).

25 S. K. Lee and C. W. Ahn, Probing of 2 Dimensional Confinement-Induced Structural Transitions in Amorphous Oxide Thin Film, *Sci. Rep.*, 2014, **4**(1), 1–5, DOI: [10.1038/srep04200](https://doi.org/10.1038/srep04200).

26 R. Lizárraga, E. Holmström, S. C. Parker and C. Arrouvel, Structural Characterization of Amorphous Alumina and Its Polymorphs from First-Principles XPS and NMR Calculations, *Phys. Rev. B: Condens. Matter Mater. Phys.*, 2011, **83**, 94201, DOI: [10.1103/PhysRevB.83.094201](https://doi.org/10.1103/PhysRevB.83.094201).

27 V. van Hoang and S. Kun Oh, Simulation of Structural Properties and Structural Transformation of Amorphous Al_2O_3 , *Phys. B*, 2004, **352**(1–4), 73–85, DOI: [10.1016/J.PhysB.2004.06.057](https://doi.org/10.1016/J.PhysB.2004.06.057).

28 G. Gutiérrez and B. Johansson, Molecular Dynamics Study of Structural Properties of Amorphous Al_2O_3 , *Phys. Rev. B: Condens. Matter Mater. Phys.*, 2002, **65**(10), 104202, DOI: [10.1103/PhysRevB.65.104202](https://doi.org/10.1103/PhysRevB.65.104202).

29 M. Aykol and K. A. Persson, *Oxidation Protection with Amorphous Surface Oxides: Thermodynamic Insights from Ab Initio Simulations on Aluminum*, 2018, DOI: [10.1021/acsami.7b14868](https://doi.org/10.1021/acsami.7b14868).

30 P. Lamparter and R. Kniep, Structure of Amorphous Al_2O_3 , *Phys. B*, 1997, **234**–236, 405–406, DOI: [10.1016/S0921-4526\(96\)01044-7](https://doi.org/10.1016/S0921-4526(96)01044-7).

31 R. L. Puurunen, Surface Chemistry of Atomic Layer Deposition: A Case Study for the Trimethylaluminum/Water Process, *J. Appl. Phys.*, 2005, **97**(12), 121301, DOI: [10.1063/1.1940727](https://doi.org/10.1063/1.1940727).

32 S. M. George, Atomic Layer Deposition: An Overview, *Chem. Rev.*, 2009, **110**(1), 111–131, DOI: [10.1021/CR900056B](https://doi.org/10.1021/CR900056B).

33 Y. Zhao, M. Amirmaleki, Q. Sun, C. Zhao, A. Codiretti, L. v. Goncharova, C. Wang, K. Adair, X. Li, X. Yang, F. Zhao, R. Li, T. Filleter, M. Cai and X. Sun, Natural SEI-Inspired Dual-Protective Layers via Atomic/Molecular Layer Deposition for Long-Life Metallic Lithium Anode, *Matter*, 2019, **1**(5), 1215–1231, DOI: [10.1016/J.MATT.2019.06.020](https://doi.org/10.1016/J.MATT.2019.06.020).

34 E. M. Lotfabad, P. Kalisvaart, K. Cui, A. Kohandehghan, M. Kupsta, B. Olsen and D. Mitlin, ALD TiO_2 Coated Silicon Nanowires for Lithium Ion Battery Anodes with Enhanced Cycling Stability and Coulombic Efficiency, *Phys. Chem. Chem. Phys.*, 2013, **15**(32), 13646–13657, DOI: [10.1039/C3CP52485J](https://doi.org/10.1039/C3CP52485J).

35 Y. Zhao, L. V. Goncharova, A. Lushington, Q. Sun, H. Yadegari, B. Wang, W. Xiao, R. Li and X. Sun, Superior Stable and Long Life Sodium Metal Anodes Achieved by Atomic Layer Deposition, *Adv. Mater.*, 2017, **29**(18), 1606663, DOI: [10.1002/adma.201606663](https://doi.org/10.1002/adma.201606663).

36 C.-Y. Chang, K.-T. Lee, W.-K. Huang, H.-Y. Siao and Y.-C. Chang, High-Performance, Air-Stable, Low-Temperature Processed Semitransparent Perovskite Solar Cells Enabled by Atomic Layer Deposition, *Chem. Mater.*, 2015, **27**(14), 5122–5130, DOI: [10.1021/ACS.ChemMater.5B01933](https://doi.org/10.1021/ACS.ChemMater.5B01933).

37 Z. Gao and Y. Qin, Design and Properties of Confined Nanocatalysts by Atomic Layer Deposition, *Acc. Chem. Res.*, 2017, **50**(9), 2309–2316, DOI: [10.1021/ACS.Accounts.7B00266](https://doi.org/10.1021/ACS.Accounts.7B00266).

38 B. J. O'Neill, D. H. K. Jackson, J. Lee, C. Canlas, P. C. Stair, C. L. Marshall, J. W. Elam, T. F. Kuech, J. A. Dumesic and G. W. Huber, Catalyst Design with Atomic Layer Deposition, *ACS Catal.*, 2015, **5**(3), 1804–1825, DOI: [10.1021/CS501862H](https://doi.org/10.1021/CS501862H).

39 J. C. C. Chan and H. Eckert, High-Resolution ^{27}Al - ^{19}F Solid-State Double Resonance NMR Studies of $\text{AlF}_3\text{-BaF}_2\text{-CaF}_2$ Glasses, *J. Non-Cryst. Solids*, 2001, **284**(1–3), 16–21, DOI: [10.1016/S0022-3093\(01\)00373-8](https://doi.org/10.1016/S0022-3093(01)00373-8).

40 D. Massiot, F. Fayon, M. Capron, I. King, S. St', S. le Calvé, C. Calvé, B. Alonso, J.-O. Durand, B. Bujoli, Z. Gan and G. Hoatson, Modelling One-and Two-Dimensional Solid-State NMR Spectra, *Magn. Reson. Chem.*, 2002, **40**, 70–76, DOI: [10.1002/mrc.984](https://doi.org/10.1002/mrc.984).

41 G. Engelhardt and H. Koller, A Simple Procedure for the Determination of the Quadrupole Interaction Parameters and Isotropic Chemical Shifts from Magic Angle Spinning NMR Spectra of Half-Integer Spin Nuclei in Solids, *Magn. Reson. Chem.*, 1991, **29**(9), 941–945, DOI: [10.1002/MRC.1260290914](https://doi.org/10.1002/MRC.1260290914).

42 G. Czjzek, J. Fink, F. Gotz, H. Schmidt, J. M. D. Coey, J. P. Rebouillat and A. Lienard, Atomic Coordination and the Distribution of Electric Field Gradients in Amorphous Solids, *Phys. Rev. B: Condens. Matter Mater. Phys.*, 1981, **23**(2513), DOI: [10.1103/PhysRevB.23.2513](https://doi.org/10.1103/PhysRevB.23.2513).

43 G. Kresse and J. Furthmüller, Efficient Iterative Schemes for *Ab Initio* Total-Energy Calculations Using a Plane-Wave Basis Set, *Phys. Rev. B: Condens. Matter Mater. Phys.*, 1996, **54**(16), 11169, DOI: [10.1103/PhysRevB.54.11169](https://doi.org/10.1103/PhysRevB.54.11169).

44 D. J. Evans and B. L. Holian, The Nose–Hoover Thermostat, *J. Chem. Phys.*, 1998, **83**(8), 4069, DOI: [10.1063/1.449071](https://doi.org/10.1063/1.449071).

45 P. E. Blöchl, Projector Augmented-Wave Method, *Phys. Rev. B: Condens. Matter Mater. Phys.*, 1994, **50**(24), 17953, DOI: [10.1103/PhysRevB.50.17953](https://doi.org/10.1103/PhysRevB.50.17953).

46 S. J. Clark, M. D. Segall, C. J. Pickard, P. J. Hasnip, M. I. J. Probert, K. Refson and M. C. Payne, First Principles Methods Using CASTEP, *Z. Kristallogr. - Cryst. Mater.*, 2005, **220**(5–6), 567–570, DOI: [10.1524/zkri.220.5.567.65075](https://doi.org/10.1524/zkri.220.5.567.65075).

47 C. J. Pickard and F. Mauri, All-Electron Magnetic Response with Pseudopotentials: NMR Chemical Shifts, *Phys. Rev. B: Condens. Matter Mater. Phys.*, 2001, **63**(24), 245101, DOI: [10.1103/PhysRevB.63.245101](https://doi.org/10.1103/PhysRevB.63.245101).

48 M. Bak, J. T. Rasmussen and N. S. I. M. P. S. O. N. Nielsen, A General Simulation Program for Solid-State NMR Spectroscopy, *J. Magn. Reson.*, 2000, **147**(2), 296–330, DOI: [10.1006/JMRE.2000.2179](https://doi.org/10.1006/JMRE.2000.2179).

49 S.-P. Gao, C. J. Pickard, A. Perlov and V. Milman, Core-Level Spectroscopy Calculation and the Plane Wave Pseudopotential Method, *J. Phys.: Condens. Matter*, 2009, **21**(10), 104203, DOI: [10.1088/0953-8984/21/10/104203](https://doi.org/10.1088/0953-8984/21/10/104203).

50 S. J. Clark, M. D. Segall, C. J. Pickard, P. J. Hasnip, M. I. J. Probert, K. Refson and M. C. Payne, First Principles Methods Using CASTEP, *Z. für Krist. - Cryst.*, 2005, **220**(5/6), 567–570, DOI: [10.1524/zkri.220.5.567.65075](https://doi.org/10.1524/zkri.220.5.567.65075).



51 R. J. Nicholls, A. J. Morris, C. J. Pickard and J. R. Yates, OptaDOS - a New Tool for EELS Calculations, *J. Phys.: Conf. Ser.*, 2012, **371**(1), 012062, DOI: [10.1088/1742-6596/371/1/012062](https://doi.org/10.1088/1742-6596/371/1/012062).

52 A. J. Morris, R. J. Nicholls, C. J. Pickard and J. R. Yates, OptaDOS: A Tool for Obtaining Density of States, Core-Level and Optical Spectra from Electronic Structure Codes, *Comput. Phys. Commun.*, 2014, **185**(5), 1477–1485, DOI: [10.1016/j.cpc.2014.02.013](https://doi.org/10.1016/j.cpc.2014.02.013).

53 J. R. Yates, X. Wang, D. Vanderbilt and I. Souza, Spectral and Fermi Surface Properties from Wannier Interpolation, *Phys. Rev. B: Condens. Matter Mater. Phys.*, 2007, **75**(19), 195121, DOI: [10.1103/PhysRevB.75.195121](https://doi.org/10.1103/PhysRevB.75.195121).

54 T. Mizoguchi, I. Tanaka, S.-P. Gao and C. J. Pickard, First-Principles Calculation of Spectral Features, Chemical Shift and Absolute Threshold of ELNES and XANES Using a Plane Wave Pseudopotential Method, *J. Phys.: Condens. Matter*, 2009, **21**(10), 104204, DOI: [10.1088/0953-8984/21/10/104204](https://doi.org/10.1088/0953-8984/21/10/104204).

55 D. Liu, Y. Guo, L. Lin and J. Robertson, First-Principles Calculations of the Electronic Structure and Defects of Al_2O_3 , *J. Appl. Phys.*, 2013, **114**(8), 083704, DOI: [10.1063/1.4818475](https://doi.org/10.1063/1.4818475).

56 H. Momida, T. Hamada, Y. Takagi, T. Yamamoto, T. Uda and T. Ohno, Theoretical Study on Dielectric Response of Amorphous Alumina, *Phys. Rev. B*, 2006, **73**(5), 054108, DOI: [10.1103/PhysRevB.73.054108](https://doi.org/10.1103/PhysRevB.73.054108).

57 R. Lizárraga, E. Holmström, S. C. Parker and C. Arrouvel, Structural Characterization of Amorphous Alumina and Its Polymorphs from First-Principles XPS and NMR Calculations, *Phys. Rev. B: Condens. Matter Mater. Phys.*, 2011, **83**, 94201, DOI: [10.1103/PhysRevB.83.094201](https://doi.org/10.1103/PhysRevB.83.094201).

58 V. Sarou-Kanian, A. N. Gleizes, P. Florian, D. Samélor, D. Massiot and C. Vahlas, Temperature-Dependent 4-, 5- and 6-Fold Coordination of Aluminum in MOCVD-Grown Amorphous Alumina Films: A Very High Field ^{27}Al -NMR Study, *J. Phys. Chem. C*, 2013, **117**(42), 21965–21971, DOI: [10.1021/jp4077504](https://doi.org/10.1021/jp4077504).

59 S. M. Lee, D. G. Cahill and T. H. Allen, Thermal Conductivity of Sputtered Oxide Films, *Phys. Rev. B: Condens. Matter Mater. Phys.*, 1995, **52**(1), 253, DOI: [10.1103/PhysRevB.52.253](https://doi.org/10.1103/PhysRevB.52.253).

60 A. Mavrić, M. Valant, C. Cui and Z. M. Wang, Advanced Applications of Amorphous Alumina: From Nano to Bulk, *J. Non-Cryst. Solids*, 2019, **521**, 119493, DOI: [10.1016/j.jnoncrysol.2019.119493](https://doi.org/10.1016/j.jnoncrysol.2019.119493).

61 M. Haouas, F. Taulelle and C. Martineau, Recent Advances in Application of ^{27}Al NMR Spectroscopy to Materials Science, *Prog. Nucl. Magn. Reson. Spectrosc.*, 2016, **94–95**, 11–36, DOI: [10.1016/j.pnmrs.2016.01.003](https://doi.org/10.1016/j.pnmrs.2016.01.003).

62 J. D. Kenneth, M. MacKenzie and E. Smith, ^{27}Al NMR, *Pergamon Mater. Ser.*, 2002, **6**(C), 271–330, DOI: [10.1016/S1470-1804\(02\)80006-2](https://doi.org/10.1016/S1470-1804(02)80006-2).

63 L. Martínez, R. Andrade, E. G. Birgin and J. M. Martínez, PACKMOL: A Package for Building Initial Configurations for Molecular Dynamics Simulations, *J. Comput. Chem.*, 2009, **30**(13), 2157–2164, DOI: [10.1002/jcc.21224](https://doi.org/10.1002/jcc.21224).

64 S. K. Lee, S. Y. Park, Y. S. Yi and J. Moon, Structure and Disorder in Amorphous Alumina Thin Films: Insights from High-Resolution Solid-State NMR, *J. Phys. Chem. C*, 2010, **114**(32), 13890–13894, DOI: [10.1021/JP105306R](https://doi.org/10.1021/JP105306R).

65 M. Kaushik, C. Leroy, Z. Chen, D. Gajan, E. Willinger, C. R. Mü Ller, F. Fayon, D. Massiot, A. Fedorov, C. Copéret, A. Lesage and P. Florian, Atomic-Scale Structure and Its Impact on Chemical Properties of Aluminum Oxide Layers Prepared by Atomic Layer Deposition on Silica, *Chem. Mater.*, 2021, **33**, 3348, DOI: [10.1021/acs.chemmater.1c00516](https://doi.org/10.1021/acs.chemmater.1c00516).

66 U. Werner-Zwanziger, A. L. Paterson and J. W. Zwanziger, The Czjzek Distribution in Solid-State NMR: Scaling Properties of Central and Satellite Transitions, *J. Non-Cryst. Solids*, 2020, **550**, 120383, DOI: [10.1016/J.JNONCrysOL.2020.120383](https://doi.org/10.1016/J.JNONCrysOL.2020.120383).

67 D. Fenzke, D. Freude, T. Fröhlich and J. Haase, NMR Intensity Measurements of Half-Integer Quadrupole Nuclei, *Chem. Phys. Lett.*, 1984, **111**(1–2), 171–175, DOI: [10.1016/0009-2614\(84\)80458-3](https://doi.org/10.1016/0009-2614(84)80458-3).

68 L. A. O'Dell, S. L. P. Savin, A. v. Chadwick and M. E. Smith, A ^{27}Al , ^{29}Si , 25 Mg and ^{17}O NMR Investigation of Alumina and Silica Zener Pinned, Sol-Gel Prepared Nanocrystalline ZrO_2 and MgO , *Faraday Discuss.*, 2006, **134**, 83–102, DOI: [10.1039/B601928E](https://doi.org/10.1039/B601928E).

69 J. Ren, L. Zhang and H. Eckert, Medium-Range Order in Sol-Gel Prepared $\text{Al}_2\text{O}_3\text{-SiO}_2$ Glasses: New Results from Solid-State NMR, *J. Phys. Chem. C*, 2014, **118**(9), 4906–4917, DOI: [10.1021/JP412774H](https://doi.org/10.1021/JP412774H).

70 D. Waroquier, X. Gonze, G.-M. Rignanese, C. Welker-Nieuwoudt, F. Rosowski, M. Göbel, S. Schenk, P. Degelmann, R. André, R. Glaum and G. Hautier, Statistical Analysis of Coordination Environments in Oxides, *Chem. Mater.*, 2017, **29**(19), 8346–8360, DOI: [10.1021/ACS.ChemMater.7B02766](https://doi.org/10.1021/ACS.ChemMater.7B02766).

71 C. Bonhomme, C. Gervais, F. Babonneau, C. Coelho, F. Pourpoint, T. Azaïs, S. E. Ashbrook, J. M. Griffin, J. R. Yates, F. Mauri and C. J. Pickard, First-Principles Calculation of NMR Parameters Using the Gauge Including Projector Augmented Wave Method: A Chemists Point of View, *Chem. Rev.*, 2012, **112**(11), 5733–5779, DOI: [10.1021/cr300108a](https://doi.org/10.1021/cr300108a).

72 D. R. Neuville, L. Cormier and D. Massiot, Al Environment in Tectosilicate and Peraluminous Glasses: A ^{27}Al MQ-MAS NMR, Raman, and XANES Investigation, *Geochim. Cosmochim. Acta*, 2004, **68**(24), 5071–5079, DOI: [10.1016/j.gca.2004.05.048](https://doi.org/10.1016/j.gca.2004.05.048).

73 J. A. van Bokhoven, A. M. J. van der Eerden and D. C. Koningsberger, Three-Coordinate Aluminum in Zeolites Observed with In Situ X-Ray Absorption Near-Edge Spectroscopy at the Al K-Edge: Flexibility of Aluminum Coordinations in Zeolites, *J. Am. Chem. Soc.*, 2003, **125**(24), 7435–7442, DOI: [10.1021/JA0292905](https://doi.org/10.1021/JA0292905).

74 D. Cabaret and C. Brouder, Origin of the Pre-Edge Structure at the Al K-Edge: The Role of Atomic Vibrations, *J. Phys.: Conf. Ser.*, 2009, **190**(1), 012003, DOI: [10.1088/1742-6596/190/1/012003](https://doi.org/10.1088/1742-6596/190/1/012003).



75 A. B. Altman, C. D. Pemmaraju, S. Alayoglu, J. Arnold, C. H. Booth, A. Braun, C. E. Bunker, A. Herve, S. G. Minasian, D. Prendergast, D. K. Shuh and T. Tyliszczak, Chemical and Morphological Inhomogeneity of Aluminum Metal and Oxides from Soft X-Ray Spectromicroscopy, *Inorg. Chem.*, 2017, **56**(10), 5710–5719, DOI: [10.1021/ACS.INORGCHEM.7B00280/SUPPL_FILE/IC7B00280_SI_001.PDF](https://doi.org/10.1021/ACS.INORGCHEM.7B00280/SUPPL_FILE/IC7B00280_SI_001.PDF).

76 J. Podder, J. Lin, W. Sun, S. M. Botis, J. Tse, N. Chen, Y. Hu, D. Li, J. Seaman and Y. Pan, Iodate in Calcite and Vaterite: Insights from Synchrotron X-Ray Absorption Spectroscopy and First-Principles Calculations, *Geochim. Cosmochim. Acta*, 2017, **198**, 218–228, DOI: [10.1016/J.GCA.2016.11.032](https://doi.org/10.1016/J.GCA.2016.11.032).

77 Y. Mao, X. X. Liang, G. J. Zhao and T. L. Song, The Structural and Optical Properties of Ternary Mixed Crystals $\text{In}_x\text{Ga}_{1-x}\text{As}$ with Zinc-Blende Structure by First-Principle Calculations, *Phys. B*, 2019, **569**, 87–95, DOI: [10.1016/J.PHYSB.2019.05.042](https://doi.org/10.1016/J.PHYSB.2019.05.042).

78 M. Bugnet, M. Jaouen, V. Mauchamp, T. Cabioch and G. Hug, Experimental and First-Principles Investigation of the Electronic Structure Anisotropy of Cr_2AlC , *Phys. Rev. B: Condens. Matter Mater. Phys.*, 2014, **90**(19), 195116, DOI: [10.1103/PhysRevB.90.195116](https://doi.org/10.1103/PhysRevB.90.195116).

79 Y. Shen, X. Yang, Y. Bian, S. Liu, K. Tang, R. Zhang, Y. Zheng and S. Gu, First Principles Study on the Structural Stability and Optoelectronic Properties of $\text{In}_x\text{Ga}_{1-x}\text{As}$ Materials with Different Indium Component, *Mater. Res. Express*, 2018, **5**(1), 015912, DOI: [10.1088/2053-1591/AAA7A8](https://doi.org/10.1088/2053-1591/AAA7A8).

80 E. O. Filatova and A. S. Konashuk, Interpretation of the Changing the Band Gap of Al_2O_3 Depending on Its Crystalline Form: Connection with Different Local Symmetries, *J. Phys. Chem. C*, 2015, **119**(35), 20755–20761, DOI: [10.1021/ACS.JPCC.5B06843](https://doi.org/10.1021/ACS.JPCC.5B06843).

81 V. Deringer, N. Bernstein, A. Bartók, M. Cliffe, R. Kerber, L. Marbella, C. Grey, S. Elliott and G. Csányi, Realistic Atomistic Structure of Amorphous Silicon from Machine-Learning-Driven Molecular Dynamics, *J. Phys. Chem. Lett.*, 2018, **9**(11), 2879–2885, DOI: [10.1021/ACS.JPCLett.8B00902](https://doi.org/10.1021/ACS.JPCLett.8B00902).

82 K. Shimoda, K. Koganei, T. Takeuchi, T. Matsunaga, M. Murakami, H. Sakaebi, H. Kobayashi and E. Matsubara, Structural Characterization of an Amorphous VS_4 and Its Lithiation/Delithiation Behavior Studied by Solid-State NMR Spectroscopy, *RSC Adv.*, 2019, **9**(41), 23979–23985, DOI: [10.1039/C9RA04338A](https://doi.org/10.1039/C9RA04338A).

83 S. Yan, K. P. Abhilash, L. Tang, M. Yang, Y. Ma, Q. Xia, Q. Guo, H. Xia, S. H. Yan, L. Y. Tang, M. Yang, Y. F. Ma, Q. Y. Xia, Q. B. Guo and H. Xia, Research Advances of Amorphous Metal Oxides in Electrochemical Energy Storage and Conversion, *Small*, 2019, **15**(4), 1804371, DOI: [10.1002/SMLL.201804371](https://doi.org/10.1002/SMLL.201804371).

84 X. Han, G. Wu, J. Du, J. Pi, M. Yan and X. Hong, Metal and Metal Oxide Amorphous Nanomaterials towards Electrochemical Applications, *Chem. Commun.*, 2021, **58**(2), 223–237, DOI: [10.1039/D1CC04141J](https://doi.org/10.1039/D1CC04141J).

